

THE CONNECTION BETWEEN STAR FORMATION RATE AND DARK MATTER HALO MASS IN THE EPOCH OF REIONIZATION

FELIPE L. GOMEZ-CORTES, JAIME E. FORERO-ROMERO

Departamento de Física, Universidad de los Andes, Cra. 1 No. 18A-10, Edificio Ip, Bogotá, Colombia

Submitted for publication in *ApJ*

ABSTRACT

We present updated constraints on the relationship between the star formation rate and dark matter halo mass at redshift $z \sim 6$. The observational basis for our work is the restframe UV luminosity function data obtained with HST, CFHTLS, Subaru and UKIRT. The constraints are based on an abundance matching methodology to the observational data using cosmological N-body simulations. The relationship between halo mass and star formation rate follows a double power law. We also take into account the influence on the results of the dust extinction scaling derived from observations by Bouwens et al. (2012). Taking advantage of a wide dynamical range in observations and simulations we manage to constrain the free parameters of our model for halos in the mass range $10^{10} M_{\odot} < M_h < 10^{13} M_{\odot}$. We find that including dust extinction improves the match with observations. Finally, we compare these results against the prediction of abundance matching methods (to the stellar mass), a semi-analytic model of galaxy formation (GALFORM) and a hydrodynamical simulation (Illustris).

Subject headings: galaxies: high-redshift — methods: numerical

1. INTRODUCTION

All magnitudes are in AB system.

2. OBSERVATIONAL CONSTRAINTS

We use information compiled in four different publications. All of them select galaxy candidates at $z \sim 6$ using the drop-out technique (Steidel et al. 1996). In what follows we describe the relevant details of each reference.

2.1. Bouwens et al. 2015

Bouwens et al. (2015) presented results from a compilation of observations taken with the Advanced Camera for Surveys (ACS) and near-infrared Wide Field Camera 3 (WFC3/IR) since 2002 through 2012. The survey includes the following fields of view. XDF, HUDF09-1, HUDF09-2, CANDELS-S/Deep, CANDELS-S/Wide, ERS, CANDELS-N/Deep, CANDELS-N/Wide, CANDELS-UDS, CANDELS-COSMOS and CANDELS-EGS.

The total survey area is 740.8 arcmin^2 over five different lines of sight, with a total estimated volume of $1.8 \times 10^6 \text{ Mpc}^3$ comoving. The limiting magnitude ranges between $\sim 27.5 \text{ mag}$ in CANDELS-EGS and $\sim 30 \text{ mag}$ in the deepest field (XDF). The total number of $z = 6$ LBG candidates is 940, most of them in the faint end of the LF given the relatively small survey volume. The restframe UV magnitudes for these candidates are in the range. $-22.52 \leq M_{1600} \leq -16.77$. The estimated Schechter parameters: $\phi^* = (0.33_{-0.10}^{+0.15}) \times 10^{-3} \text{ Mpc}^{-3}$, $M_{1600}^* = -21.16 \pm 0.20$ and $\alpha = -1.91 \pm 0.09$.

2.2. Finkelstein et al. 2014

Finkelstein et al. (2014) worked also with HST data. They used results from the HUDF, CANDELS and GOODS fields, along with two of the Hubble Frontier Fields (HFF) of deep parallel observations (unlensed

fields) near the Abell 2744 and MACS J0416.1-2403 clusters. The HFF uses the ACS and the WFC3/IR with the same filters aforementioned except z_{850} . The total survey area is around $\sim 300 \text{ arcmin}^2$ with a total estimated volume of $8 \times 10^5 \text{ Mpc}^{-3}$. There are 706 photometric candidates at redshift 6 defined as the interval $5.5 < z < 6.5$. The Schechter function parameters estimated for this data set are $\phi^* = (1.86_{-0.80}^{+0.94}) \times 10^{-4} \text{ Mpc}^{-3}$, $M_{1600}^* = -21.1_{-0.31}^{+0.25}$ and $\alpha = -2.02_{-0.10}^{+0.10}$.

2.3. Willott et al. 2013

Willott et al. (2013) presented results from the sixth release of the Canada-France-Hawaii Telescope Legacy Survey (CFHTLS). The observations were performed over four separated fields covering a total area $\sim 4 \text{ deg}^2$ giving a survey volume of $\sim 1 \times 10^7 \text{ Mpc}^3$, which is over one order of magnitude larger than the compilations by Bouwens et al. (2015) and Finkelstein et al. (2014).

They performed optical observations with MegaCam. Their main selection criteria was that all objects must be brighter than magnitude $z' = 25.3$. The final number of LBGs founded was 40. Moreover, they get spectroscopic confirmation for 7 candidates using GMOS spectrograph on the Gemini Telescopes, which has a $\ll 5.5$ -square arcmin field of view.

The survey was focused on the most luminous LBGs. The full LF at $z = 6$ cannot be obtained as in other studies, however its large volume allows constraints on the bright end. The LF Schechter parameters are calculated in the magnitude range $-20.5 > M_{1350} > -22.5$.

2.4. McLure et al. 2009

McLure et al. (2009) used data obtained with the the United Kingdom Infrared Telescope (UKIRT) in the near-IR imaging and Subaru Telescope for the optical imaging. They covered 2268 arcmin^2 for a volume $\sim 3 \times 10^6 \text{ Mpc}^3$. The UKIRT was equipped with the WFCAM using *JK* filters, while Subaru was equipped

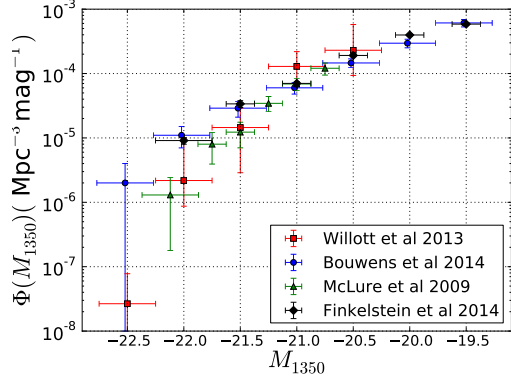


FIG. 1.— Observational data from Bouwens et al. (2015); Finkelstein et al. (2014); McLure et al. (2009) and Willott et al. (2013), with the Suprime-Cam with the $BVRiz'$ filters. All candidates were brighter than $z' = 26$. The UV rest frame magnitude range is $-22.4 \leq M_{1500} \leq -20.6$. The LF was calculated using the maximum likelihood estimator of Schmidt (1968). Their analysis gave a total number of 104 LBG candidates in the redshift range $5.7 \leq z \leq 6.3$. They reported the following values for the Schechter function $\phi^* = (1.8 \pm 0.5) \times 10^{-3} \text{Mpc}^{-3}$, $M_{1500}^* = -20.04 \pm 0.12$ and $\alpha = -1.71 \pm 0.11$.

2.5. Dust Attenuation

Dust in star forming galaxies can attenuate the UV intrinsic luminosity. Although relatively uncertain compared to studies in the local universe, there are constraints on the extinction level in LBGs at $z = 6$.

These studies are based on the UV Spectral slope β correlation with extinction. This index can be defined approximating by a power-law the shape the spectral flux f as function of the wavelength $\lambda f \propto \lambda^\beta$. The relation for attenuation at 1600\AA is $A_{1600} = 4.43 + 1.99\beta$, with A_{1600} in magnitude units Meurer et al. (1999).

Bouwens et al. (2012) uses the fluxes on different bands to estimate β on each LBG candidate found with $z \sim 4 - 7$. At $z = 6$ they found a linear relation between β and M_{UV} :

$$\langle \beta \rangle = \frac{d\beta}{dM_{UV}} (M_{UV,AB} + 19.5) + \beta_{M_{UV}=-19.5}, \quad (1)$$

with $\beta_{M_{UV}=-19.5} = -2.20$ and $d\beta/dM_{UV} = -0.21$ at $z = 5.9$. We use these relationships to modify the intrinsic UV luminosity values.

3. THEORETICAL, NUMERICAL AND STATISTICAL FRAMEWORK

3.1. The Abundance Matching Methodology

We use an abundance matching approach to find the relationship between dark matter halo mass and star formation rate. This approach has been used to link stellar and dark matter masses. Here we extend it to constraint star formation rate properties at high redshift.

The starting point for this method is a population of dark matter halos. To each halo we assign a UV luminosity according to the following parameterization.

$$L_{UV}(M) = L_0 M \left[\left(\frac{M}{M_0} \right)^{-\beta} + \left(\frac{M}{M_0} \right)^{\gamma} \right]^{-1}, \quad (2)$$

where M is the DM mass, L_0 is a normalization constant, M_0 is the critical mass where the luminosity function has a slope change, β and γ are two slopes corresponding to the faint and bright end, respectively. We note that this equation has the same functional dependence suggested by Moster et al. (2010) to link stellar and dark matter masses.

Once each halo has a UV luminosity we also have the option to include an extinction correction (as described in SS2.5) in order to modify this intrinsic luminosity value. From these UV values we build the LF. The free parameters in Eq. (2) are determined by requiring that the abundance matching LF follows the observational constraints. Then we use the following relationship between UV luminosity and Star Formation Rate (Madau et al. 1998; Kennicutt 1998)

$$\text{SFR} (M_\odot \text{yr}^{-1}) = 1.4 \times 10^{-28} L_\nu (\text{erg s}^{-1} \text{Hz}^{-1}), \quad (3)$$

to finally link SFR with DM halo mass.

3.2. N-body Simulations and Halo Catalogs

Cosmological N-body simulations are the source of the dark matter halo populations. We use two different simulations to cover the wide dynamical range explored by the observations: Big MultiDark Planck (MDPL) and Planck Bolshoi (P-Bolshoi). Both simulations use 2013 Planck cosmology defined by the following parameters: $\Omega_M = 0.307$, $\Omega_B = 0.048$, $\Omega_\Lambda = 0.730$, $\sigma_8 = 0.829$, $n_s = 0.96$ and $H_0 = 67.8$.

The MDPL run is a N-body dark matter only simulation based on the L-Gadget2 code. The simulated volume is a cubic box of 1Gpc h^{-1} on a side. It has 3840^3 dark matter particles mass of $1.51 \times 9 M_\odot h^{-1}$. The DMH Catalog at $z = 6$ contains $\sim 10.9 \times 10^7$ halos, to avoid incompleteness in the low mass end, halos with mass below $10^{10.3} M_\odot h^{-1}$ are rejected. We split this large volume into 64 smaller cubic boxes of $250 h^{-1} \text{Mpc}$ on a side (similar volume to the observations by Willott et al. (2013)) to study the influence of cosmic variance.

The P-Bolshoi simulation...

We obtained the data from the public database¹ (Riebe et al. 2013).

3.3. Constraining the Free Parameters

We use a Markov Chain Monte Carlo (MCMC) methodology to constraint the free parameters in Eq. (2). We use a Metropolis-Hastings algorithm to build the MC chains on the four parameters. We performed 10^5 MCMC steps with 10^4 additional initial burn-out iterations.

To explore the likelihood $\mathcal{L} \propto \exp(-\chi^2)$ we consider the following χ^2 .

$$\chi^2 = \sum_{i=0}^n \frac{(\log \Phi_{i,obs} - \log \Phi_{i,th})^2}{2\sigma_i^2}, \quad (4)$$

defined over each LF magnitude bin.

We treat each dataset (Bouwens, Finkelstein, Willott and McLure) separately to join at the end the posteriors. The size and halo resolution of the computational boxes

¹ <http://www.multidark.org>

Parameter	Dust Att.		No-Dust Att.	
	MCMC	C.Var.	MCMC	C.Var.
$\log_{10}(L_0/L_\odot)$	$18.07^{+0.10}_{-0.06}$	0.03	$17.81^{+0.12}_{-0.08}$	0.02
$\log_{10}(M_0/M_\odot)$	$11.19^{+0.67}_{-0.03}$	0.07	$11.12^{+0.58}_{-0.24}$	0.06
β	$1.480^{+0.11}_{-1.28}$	0.18	$1.44^{+0.16}_{-1.35}$	0.18
$\gamma \times 0.1$	$4.028^{+3.01}_{-0.82}$	0.58	$5.18^{+2.36}_{-0.59}$	0.46

TABLE 1

BEST FIT PARAMETERS TO THE WILLOTT DATA WITH AND WITHOUT DUST ATTENUATION OVER 64 SMALL BOXES. MEAN BEST VALUE ESTIMATED WITH MCMC, MEAN 1σ CONFIDENCE INTERVAL AND COSMIC VARIANCE (C.VAR.)

is coarse for the case of Willott and fine for the other datasets. We perform two kinds of MCMC explorations with and without considering dust extinctions. We impose the following priors over the parameters $0 \leq \alpha \leq 2.0$ and $\gamma \geq 0$.

4. RESULTS

4.1. Willott

We use 64 cubic boxes of $250h^{-1}\text{Mpc}$ on a side to fit the LF data from Willott et al. (2013). We use the Likelihood Ratio criterion ($\mathcal{LR} = 0.5$) to define the 1σ confidence interval for our parameters.

M_0 does not change with and without extinction. cases (they are compatible within the error bars), the turnover point corresponds to the same mass. γ and L_0 shown

a significant difference in booth cases. β is hard to constraint in booth cases. The paramerer was limited to vary in the range form 0.0 to 1.6. 1σ region covers the whole range.

The UV luminosity model (eqn. 2) that we have chosen can be divided in two regimes; high mass regime (with $M > M_0$) and low mass regime (with $M < M_0$).

The observational dataset from Willott are in the high mass regime with one point in the low mass regime. It makes makes hard to impose restrictions over β , but the other three parameters can be well defined.

We also compare the likelihood of the two cases on each individual small box. The Dust Attenuation model is more accurate than the No-Dust Attenuation model in most of the cases as is shown in the figure 2.

To study cosmic variance effects, we compared the best fit parameters of each box and its likelihood value. We found that cosmic variance effects are less significant in best fit parameters than MCMC parameter estimation itself.

5. DISCUSSION

6. CONCLUSIONS

ACKNOWLEDGMENTS

Acknowledgments...

The observational datasets were retrieved using GAVO-DEXTER².

REFERENCES

- Behroozi, P. S., Wechsler, R. H., & Conroy, C. 2013, ApJ, 770, 57
- Bouwens, R. J., Illingworth, G. D., Oesch, P. A., Franx, M., Labbé, I., Trenti, M., van Dokkum, P., Carollo, C. M., González, V., Smit, R., & Magee, D. 2012, ApJ, 754, 83
- Bouwens, R. J., Illingworth, G. D., Oesch, P. A., Trenti, M., Labbé, I., Bradley, L., Carollo, M., van Dokkum, P. G., Gonzalez, V., Holwerda, B., Franx, M., Spitler, L., Smit, R., & Magee, D. 2015, ApJ, 803, 34
- Finkelstein, S. L., Ryan, Jr., R. E., Papovich, C., Dickinson, M., Song, M., Somerville, R., Ferguson, H. C., Salmon, B., Giavalisco, M., Koekemoer, A. M., Ashby, M. L. N., Behroozi, P., Castellano, M., Dunlop, J. S., Faber, S. M., Fazio, G. G., Fontana, A., Grogin, N. A., Hathi, N., Jaacks, J., Kocevski, D. D., Livermore, R., McLure, R. J., Merlin, E., Mobasher, B., Newman, J. A., Rafelski, M., Tilvi, V., & Willner, S. P. 2014, ArXiv e-prints
- Kennicutt, Jr., R. C. 1998, ARA&A, 36, 189
- Madau, P., Pozzetti, L., & Dickinson, M. 1998, ApJ, 498, 106
- McLure, R. J., Cirasuolo, M., Dunlop, J. S., Foucaud, S., & Almaini, O. 2009, MNRAS, 395, 2196
- Meurer, G. R., Heckman, T. M., & Calzetti, D. 1999, ApJ, 521, 64
- Moster, B. P., Somerville, R. S., Maulbetsch, C., van den Bosch, F. C., Macciò, A. V., Naab, T., & Oser, L. 2010, ApJ, 710, 903
- Riebe, K., Partl, A. M., Enke, H., Forero-Romero, J., Gottlöber, S., Klypin, A., Lemson, G., Prada, F., Primack, J. R., Steinmetz, M., & Turchaninov, V. 2013, Astronomische Nachrichten, 334, 691
- Schmidt, M. 1968, ApJ, 151, 393
- Steidel, C. C., Giavalisco, M., Pettini, M., Dickinson, M., & Adelberger, K. L. 1996, ApJ, 462, L17
- Willott, C. J., McLure, R. J., Hibon, P., Bielby, R., McCracken, H. J., Kneib, J.-P., Ilbert, O., Bonfield, D. G., Bruce, V. A., & Jarvis, M. J. 2013, AJ, 145, 4

² <http://dc.zah.uni-heidelberg.de/dexter/ui/ui/custom>

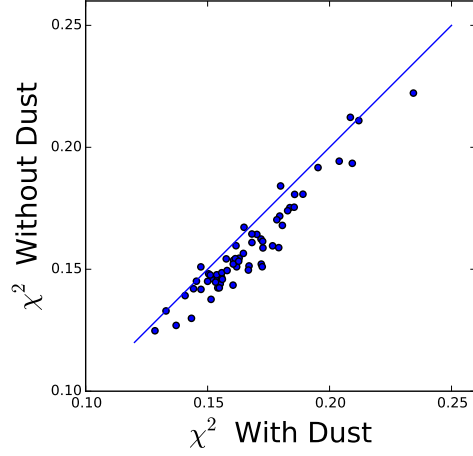


FIG. 2.— Best fit to Willott comparison between the two models. Each point represent χ^2 calculated over each small-box. The solid line represents the ratio 1:1

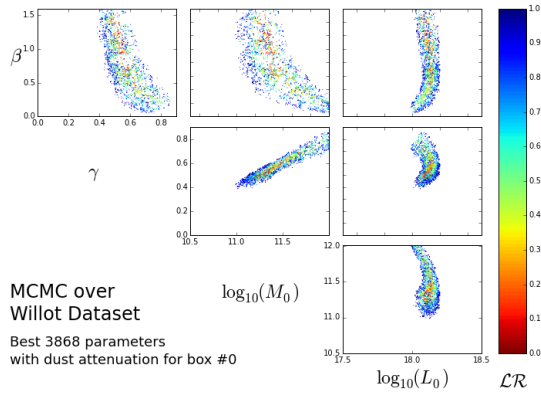


FIG. 3.— Parameter dispersion fitting the Willott with the Dust Attenuation model. 1σ is defined by the likelihood ratio between 0.0 (red) and 0.5 (green)

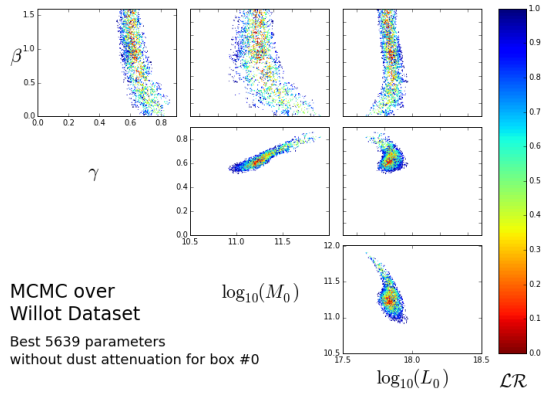


FIG. 4.— Parameter dispersion fitting the Willott with the No-Dust Attenuation model. 1σ is defined by the likelihood ratio between 0.0 (red) and 0.5 (green)

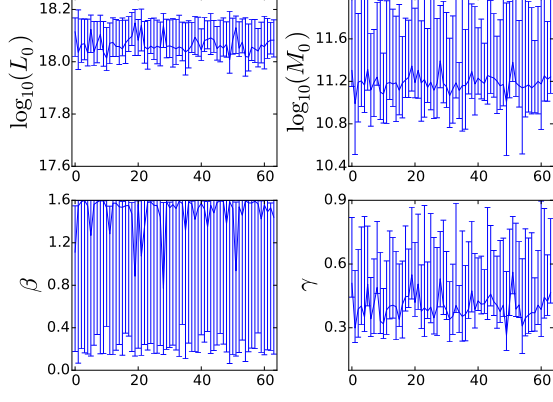


FIG. 5.— Individual small-box parameter estimation with dust attenuation: Best fit values to the Willott data set (solid line) and 1σ confidence interval using likelihood ratio $\mathcal{LR} = 0.5$. The x axis corresponds to the box number.

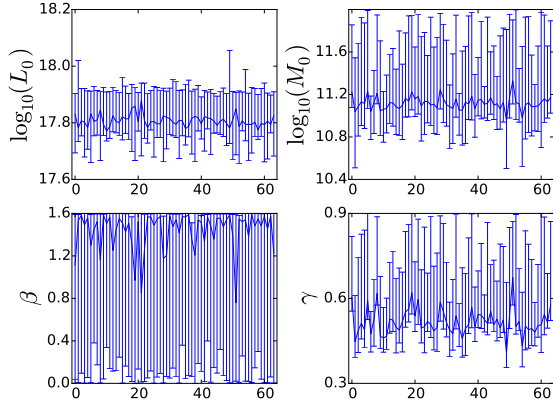


FIG. 6.— Individual small-box parameter estimation with no-dust attenuation: Best fit values to the Willott data set (solid line) and 1σ confidence interval using likelihood ratio $\mathcal{LR} = 0.5$. The x axis corresponds to the box number.

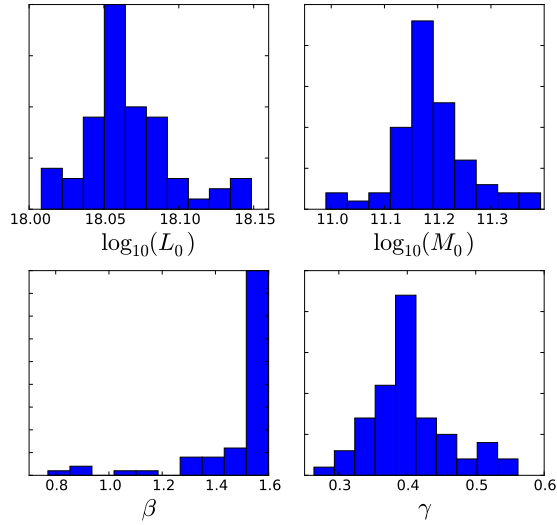


FIG. 7.— Best fit parameter distribution due to cosmic variance with Willott data in the dust attenuation model.

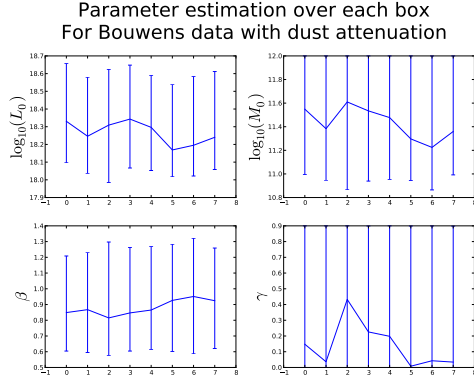


FIG. 8.— Best fit parameter distribution due cosmic variance with Bouwens data in the dust attenuation model.

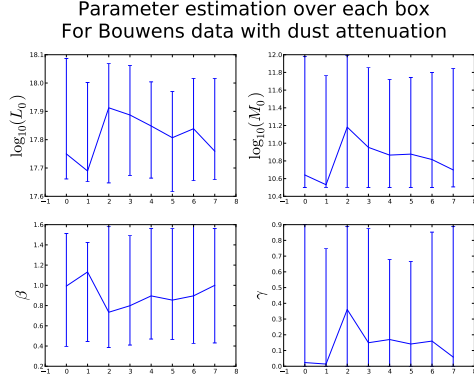


FIG. 9.— Best fit parameter distribution due cosmic variance with Bouwens data in the no-dust attenuation model.

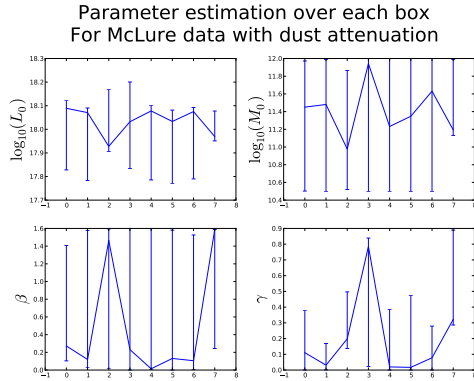


FIG. 10.— Best fit parameter distribution due cosmic variance with McLure data in the dust attenuation model.

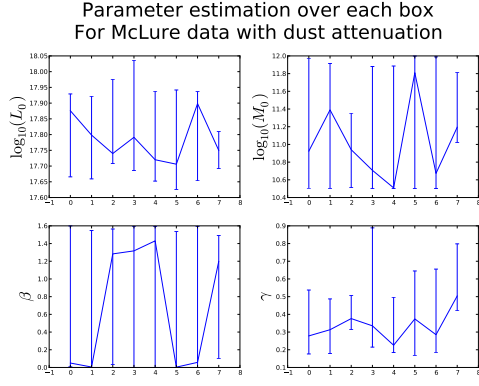


FIG. 11.— Best fit parameter distribution due cosmic variance with McLure data in the no-dust attenuation model.

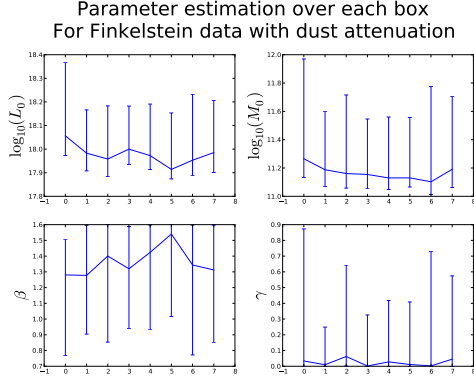


FIG. 12.— Best fit parameter distribution due cosmic variance with Finkelstein data in the dust attenuation model.

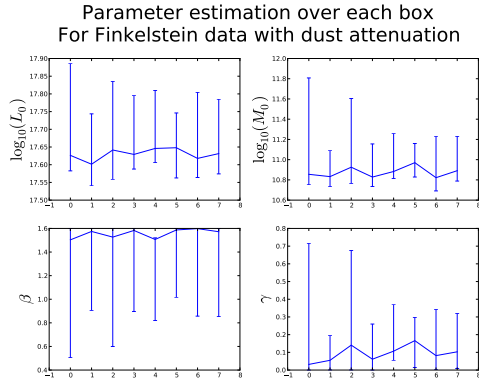


FIG. 13.— Best fit parameter distribution due cosmic variance with Finkelstein data in the no-dust attenuation model.

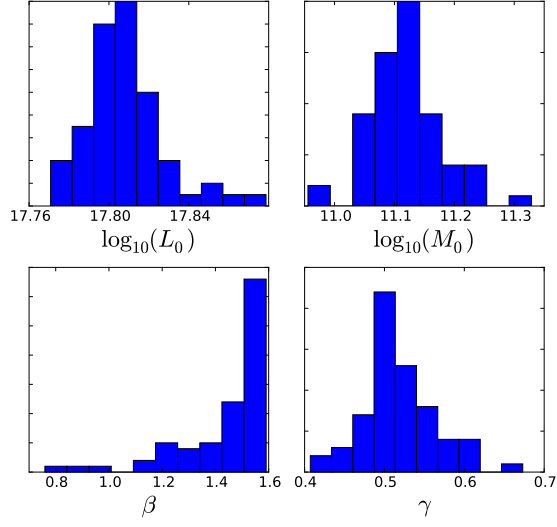


FIG. 14.— Best fit parameter distribution due cosmic variance with Willott data in the no-dust attenuation model.

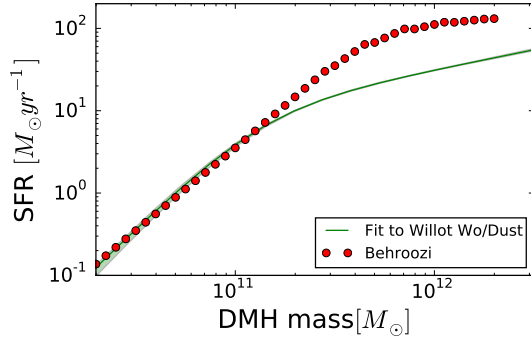


FIG. 15.— Star formation rate as function of the dark matter halo mass without dust attenuation. Solid lines represents the mean SFR value over the small boxes within 50% shaded region. Comparison with an implementation of abundance matching model (Behroozi et al. 2013).

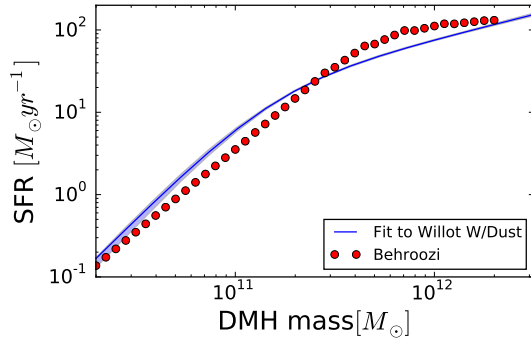


FIG. 16.— Star formation rate as function of the dark matter halo mass with dust attenuation. Solid lines represents the mean SFR value over the small boxes within 50% shaded region. Comparison with an implementation of abundance matching model (Behroozi et al. 2013).